C: Physical Processes in Nanomaterials and Nanostructures

Synthesis of Graphene Nanoribbons on a Kinked Au Surface: Revealing the Frontier Valence Band at the Brillouin Zone Center

Afaf El-Sayed, Ignacio Piquero-Zulaica, Zakaria M. Abd El-Fattah, Lukáš Kormoš, Khadiza Ali, Andrew Weber, Jens Brede, Dimas G. de Oteyza, Jorge Lobo-Checa, J. Enrique Ortega, and Martina Corso

J. Phys. Chem. C, **Just Accepted Manuscript** • DOI: 10.1021/acs.jpcc.0c02801 • Publication Date (Web): 23 Jun 2020

Synthesis of Graphene Nanoribbons on a Kinked Au Surface: Revealing the Frontier Valence Band at the Brillouin Zone Center

Afaf El-Sayed,[†,‡,¶] Ignacio Piquero-Zulaica,[*,§,‖] Zakaria M. Abd El-Fattah,[†,¶] Lukas Kormos,[⊥] Khadiza Ali,[§] Andrew Weber,[¶,§] Jens Brede,[§] Dimas G. de Oteyza,[¶,§,#] Jorge Lobo-Checa,[@] J. Enrique Ortega,[§,¶,△] and Martina Corso[*,§,¶]

†*Physics Department, Faculty of Science, Al-Azhar University, Nasr City, 11884 Cairo, Egypt*

‡*University of Science and Technology, Nanoscience Program, Zewail City of Science and Technology, October Gardens, 6th of October, 12578 Giza, Egypt*

¶*Donostia International Physics Center, 20018 Donostia-San Sebastian, Spain*

§*Centro de Física de Materiales CFM/MPC (CSIC-UPV/EHU), 20018 Donostia-San Sebastián, Spain*

‖*Physik Department E20, Technische Universität München, 85748 Garching, Germany*

⊥*Central Institute of Technology, Brno University of Technology (CEITEC-BUT), Brno, Czech Republic*

#*Ikerbasque, Basque Foundation for Science, 48013 Bilbao, Spain*

@*Instituto de Ciencia de Materiales de Aragón and Departamento de Física de la Materia Condensada, CSIC-Universidad de Zaragoza, Pedro Cerbuna 12, 50009 Zaragoza, Spain*

△*Departamento de Física Aplicada I, Universidad del País Vasco, San Sebastián, Spain*

E-mail: ipiquerozulaica@gmail.com; martina.corso@ehu.eus

Abstract

Graphene nanoribbons (GNRs) can be synthesized with atomic precision through on-surface chemistry of self-assembled organic precursors on metal surfaces. Here we examine the growth of 7-armchair GNRs (7-AGNRs) on the Au(16 14 15) vicinal surface, namely, a surface vicinal to Au(111) that features kinked steps. During the thermal activation of the polymerization and cyclodehydrogenation processes that produce the GNRs, the kinked substrate undergoes a strong step-edge reshaping, accompanied by a massive missing-row reconstruction within (111) terraces that aligns GNRs preferentially along two equivalent $[1\bar{1}0]$ directions. Using angle-resolved photoemission we are able to detect the occupied frontier band of the 7-AGNR at the center of the first Brillouin zone, as predicted by theoretical calculations. This allows to unambiguously determine the relevant 7-AGNRs band properties, namely energy and effective mass.

Introduction

Graphene nanoribbons (GNRs), that is, one-dimensional stripes of graphene, are an ideal class of carbon materials with potential use as devices' components in the next post-silicon technology. Thanks to the tunability of their electronic and structural properties, mostly determined by the atomic structure of their edge, they can be used as active elements in electronic devices, as field effect transistors,[1–3] diodes,[4] or as metallic interconnects.[5] A breakthrough in the bottom-up fabrication of atomically precise GNRs is provided by on-surface synthesis that allows growing GNRs with armchair, zigzag or chiral edges,[6–9] semiconducting GNRs with different widths and electronic bandgap sizes,[10–15] and GNRs with substitutional dopant heteroatoms[16–23] or functional groups.[24,25] Specially designed molecular precursors, once deposited on a metallic substrate, undergo thermally activated polymerization and cyclodehydrogenation to form graphene-like ribbons.[6] A great attention has been given so far to the chemical design of precursor monomers that yield high precision in the final structures, which have been mostly tested on the Au(111) surface. Nevertheless, the use of more

"exotic" or technologically relevant surface terminations and materials for GNRs growth remains highly unexplored. The surface is important in several stages of the on-surface synthesis process as in the oligomers activation, stabilization of radicals, monomers diffusion and polymerization fulfilment. Moreover, step edges, kinks, dislocations, adatoms and defects can act as catalytic active sites for the initial or guided GNRs growth.[26] Vicinal surfaces (crystals exhibiting step arrays on their surface), for example, allow synthesizing long-range ordered parallel arrays of GNRs that can be transferred to insulating surfaces maintaining their orientation, as required in efficient electronic and optoelectronic devices.[27,28]

The use of vicinal surfaces with a high density of structural kinks may provide additional flexibility to GNR growth. Atoms at kinks have lower coordination compared to the other surface neighbors, leading to a reduced thermal excitation energy. This effectively increases the presence of substrate atoms diffusing along step edges or inside terraces, and therefore the number of metal atoms readily available as catalysts for the on-surface reaction. In fact, the presence of kinks has been shown to favor dehalogenation,[29] and hence varying their density might be a good way to control the GNRs length, and favor dense arrays of GNRs with homogeneous length and orientation. Also, kinked steps can reconstruct or "roughen" without changing the bonding configuration of the step edge, allowing the step to freely "bend" on the surface plane,[30] such as to conform to a particular GNR topology (straight, chiral, or zigzag).[31] Finally, kinked single crystal surfaces can be chosen to possess a chiral structure that offers chiral discrimination, as it has been demonstrated for molecular adsorption of L- and D-cysteine on Au(17 11 9).[32] This property could drive the selective growth of only one type of chiral GNRs among the possible enantiomeric structures.[9]

Here we test the growth of semiconducting armchair graphene nanoribbons with a width of 7 carbon atoms (7-AGNRs) on the kinked Au(16 14 15) surface. We find that the presence of kinked steps leads to a lowering of the dehalogenation temperature with respect to the flat Au(111) surface, similar to the case of the corrugated Au(110).[33] Moreover, long and well aligned 7-AGNRs form, while the surface undergoes a strong reshaping of the kinked

step-edges. Besides this macroscopic steps reshaping, we also observe the reconstruction of (111) terraces into missing row structures, likely due to the presence of Au adatoms that diffuse away from the kinked steps. The ribbons' length and alignment comparable to that obtained on the Au(788) surface, allows to measure in detail the electronic structure of the 7-AGNRs by angle-resolved photoemission (ARPES). ARPES maps show the presence of the theoretically predicted, but never observed 7-AGNRs' frontier valence band at the $\bar{\Gamma}$ point in the first Brillouin Zone.[34]

Methods

Experimental methods

The experiments were performed in two different ultra-high-vacuum (UHV) systems with base pressures in the low 10^{-10} mbar range. The first system hosts a commercial Omicron variable temperature scanning tunneling microscope (VT-STM) and an ARPES setup with a high-resolution display type hemispherical electron analyzer (Phoibos150). The radiation at 21.2 eV photon energy was provided by a high-intensity monochromatic source. Energy and angular resolution were set to 40 meV and 0.1°, respectively. The sample was mounted with the manipulator and vertical analyzer slit aligned perpendicular to the step direction (i.e. perpendicular to the nominal $[11\bar{2}]$ direction), allowing us to measure a wide band dispersion range parallel to the GNR average direction by sample rotation (polar scans by manipulator rotation). For the *s*- (*p*-) polarized light, the electric field vector lies perpendicular (parallel) to the plane defined by the directions of the light incidence and sample normal, as shown in the sketch of Fig. S1 in the Supporting Information. The sample was kept at approximately 150 K during ARPES scans. STM experiments were performed at room temperature (RT). STM images were taken in constant current mode and processed with the WSXM software.[35]

In the second UHV system, X-ray photoelectron spectroscopy (XPS) experiments were performed, using a SPECS Phoibos 100 spectrometer equipped with a standard non-monochromatic

Al Kα X-ray source. Temperature dependent XPS data were acquired in 2 °C/5 minute steps during a 41 hours annealing cycle. Highly resolved spectra were measured in a subsequent experiment at the relevant sample temperatures determined from the XPS long temperature scan. XPS peaks were fitted with Doniach Sunjic functions and Shirley background.

The Au(16 14 15) single crystal was prepared by repeated cycles of sputtering (Ar^+, 0.8−1.2 keV) and annealing to about 460°C in UHV, and cleanliness and step array ordering were monitored by low energy electron diffraction (LEED), STM and ARPES. The Au(16 14 15) plane features (111) terraces and monatomic steps running along the $[11\overline{2}]$ direction, that is, steps with nominally maximum density of six-fold coordinated kink atoms. Commercially purchased 10,10'-dibromo-9,9'-bianthracene (DBBA) molecules were sublimated on the clean crystal in UHV from a Knudsen cell at 170°C. 7-AGNRs were grown on Au(16 14 15) following the recipe from Ref.,[6] which consists on depositing DBBA molecules at RT, annealing to 200°C for 5 min to induce polymerization of the molecular precursors by Ullmann coupling, and finally raising the temperature to 380°C (for 30 s) to trigger cyclodehydrogenation, and hence obtain the 7-AGNRs formation, avoiding their lateral fusion into wider nanoribbons.

Theoretical simulation of ARPES bands

The band structure of individual GNRs and its corresponding ARPES intensity were theoretically determined with the Electron Plane Wave Expansion (EPWE) method. This approach has been successfully applied to graphene nanostructures with comparable accuracy to results obtained from DFT calculations.[36] We define an inverted honeycomb potential landscape, where carbon atoms are represented by circles of diameter a=1.42 Å defining regions of zero potential, while a value of $\sim$ 23 eV is assigned to the hexagonally warped carbon voids. The 7-AGNR characteristic unit cell is created and the periodicity along the nanoribbon axis (y-direction) was set to 3a. Following the supercell approach, we separate ribbons in the x-direction by distances greater than 15 Å. Good convergence is achieved by terminating the potential expansion at the maximum 2D reciprocal lattice vector $g_{\max} = 20$, while the

number of plane waves used is $\sim {g_{\max}}^2$. We obtained the band structure and photoemission intensity by solving Schrödinger equation for this defined potential landscape following the procedures detailed in Ref.[36]

Results and Discussion

The Au(16 14 15) plane defines a vicinal angle of 3.1° with respect to the high symmetry (111) surface. It consists of terraces and monatomic steps running along the $[11\bar{2}]$ direction. Nominally, the steps feature a maximum density of six-fold coordinated kink atoms and the terraces present weak herring-bone-like discommensuration lines, running quasi-perpendicular to the step direction. Analysis of STM images taken at room temperature, such as the one displayed in Fig. 1a, reveals a mean step spacing [(111) terrace size] of 4.2±0.6 nm. A closer view to the step edge of the clean Au(16 14 15) surface indicates that the nominally straight step featuring six-fold coordinated kink atoms is reconstructed into periodic 120° triangular out-protrusions, likely formed by alternating close-packed {100} and {111} minifacets (Fig. 1c). Moreover, the fast Fourier transform of STM pictures (as Fig. 1a) show a regular quasi-hexagonal pattern, indicating that such periodic triangular reconstruction of the step edge is coherent between contiguous steps and extends over the entire surface.

Upon 7-AGNRs growth, the Au(16 14 15) surface undergoes a strong reshaping forming triangular protrusions with on average 15±5 nm step-edge segments, as deduced from STM images as in Fig. 1b (see also Fig. S2). High-quality 7-AGNRs grow with variable length up to 35 nm, aligned preferentially along the two equivalent $[1\bar{1}0]$ close packed substrate directions parallel to the triangular step segments (as demonstrated in Fig. S2). STM images acquired for ribbon coverage below the full layer allow one to identify a further surface reconstruction at (111) terraces in Fig. 1d. In-between individual 7-AGNRs one can observe chains of atoms along the $[1\bar{1}0]$ in-plane direction, arranged in a missing row fashion.

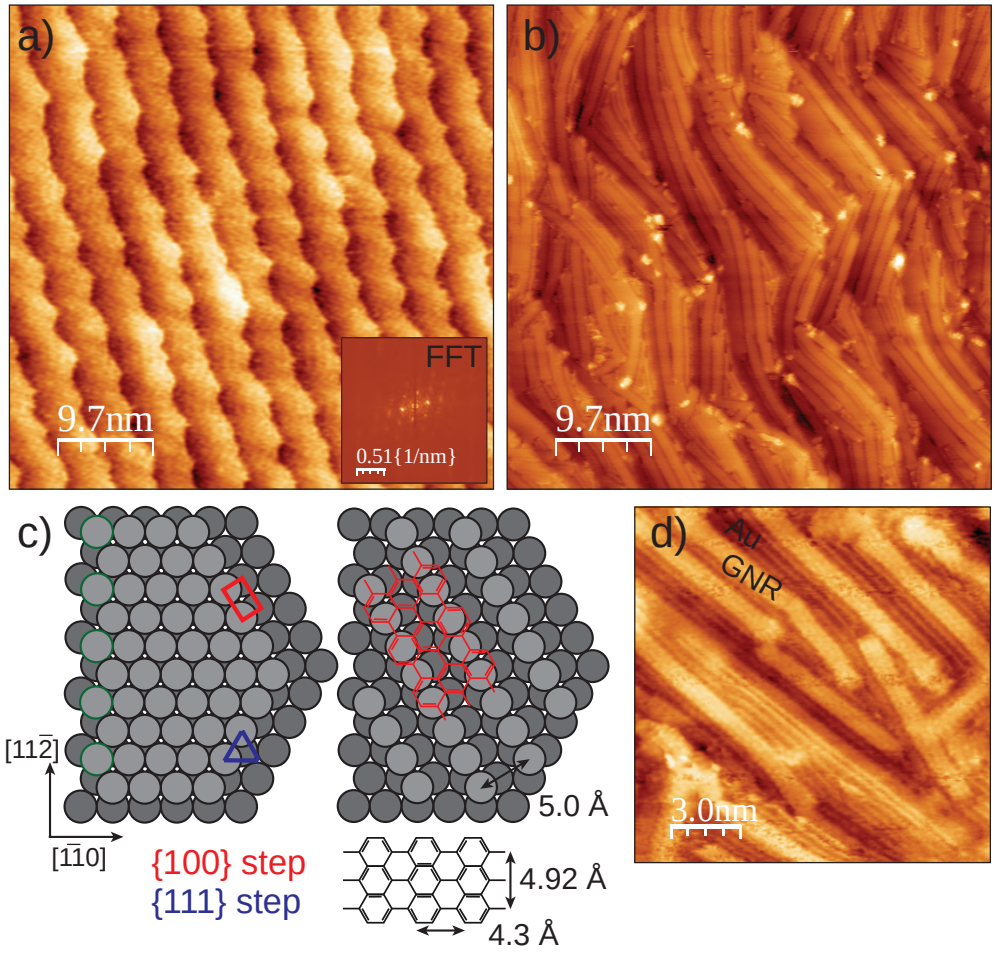

Figure 1: (a) STM image of the kinked Au(16 14 15) surface showing a coherent pattern of reconstructed steps along the [11$\bar{2}$] direction, as deduced from the hexagonal pattern in the fast Fourier transform shown in the inset. (b) Kinked surface covered by almost one single layer of 7-AGNRs. (c) On the left, model of unreconstructed (left edge) and reconstructed (right edge) steps on the kinked Au(16 14 15). The latter define 120° triangular protrusions, formed with alternating {100}- and {111}-like minifacets (red square and blue triangle, respectively). On the right, model of the atomic-row (2×1) reconstruction at (111) terraces, observed after 7-AGNRs formation. The adsorption configuration of the ribbon is shown overlaid. (d) STM image of a sample preparation with 7-AGNRs coverage lower than in (b), where the atomic row reconstruction of (111) terraces is visible in-between 7-AGNRs.

The distance between the rows is 0.48±0.03 nm (see also see Fig. S3), which corresponds to the (2×1) terrace reconstruction schematically plotted in Fig. 1c (also observed in LEED images, Fig. S4). We identify the atomic species as Au atoms that have likely diffused away from the kinked step edges due to the relatively high temperature needed to synthesize the ribbons.

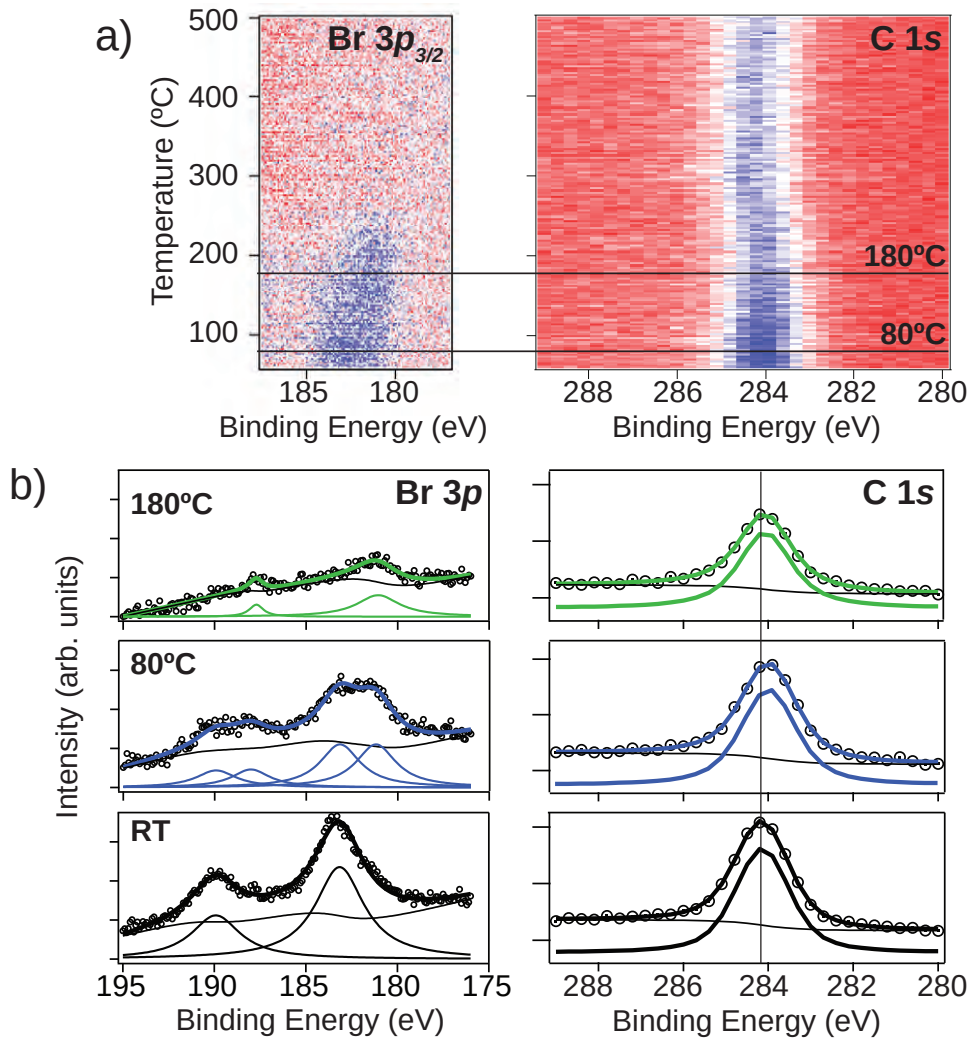

Figure 2: (a) Evolution with annealing temperature of the Br $3p_{3/2}$ and the C $1s$ core levels intensity for one layer of DBBA molecules deposited at RT on Au(16 14 15) up to 500°C. Blue and red indicate high peak intensity and intensity minimum, respectively. (b) Br $3p$ spectra (left) and C $1s$ spectra (right) with their corresponding fits taken at RT, after annealing to 80°C and after annealing to 180°C. All the spectra were recorded at RT. The vertical black line shows the C $1s$ peak position at RT resulting from the fit. Data taken in (a) is noisier than the one shown in (b) due to the necessary limitation to a single sweep per temperature scan.

To exclude that the (2×1) atomic row reconstruction arises due to trapped Br atoms, as observed in the case of polymeric chains on Au(111),[37] we performed temperature desorption XPS. In Fig. 2a we show the temperature-dependent evolution of the Br $3p_{3/2}$ and the C $1s$ core level peaks for one layer of DBBA molecules, deposited at RT, and slowly annealed up to 500°C. The binding energy of the Br $3p$ peak at RT (Fig. 2b) corresponds to the

one found for DBBA on the Au(111) surface, demonstrating that the molecules adsorb intact and homogeneously on the substrate (single Br component). By 80°C the Br 3p peak splits into two components (Fig. 2b): the metal bound peak and the organic peak (with a 2 eV higher binding energy), which suggests a partial dehalogenation of our precursor molecules. At higher temperature (180°C as shown in Fig. 2b) only isolated Br atoms may survive, indicating that all our precursor molecules have lost their Br, thereby forming a polymeric chain. The complete dehalogenation occurs at a temperature lower than in Au(111) (≈207°C), but similar to that of the more reactive corrugated Au(110) surface (≈177°C),[33] indicating an enhanced Br detachment process at the kinked surface. Above 250°C no Br atoms remain on the surface. This finding assures that the atoms trapped between GNRs are not Br but Au, since 7-AGNRs were formed on this surface upon annealing to 380°C. Note that such (2×1) reconstruction must be related in part to the kinked nature of the steps, since it was not observed in the case of GNRs grown on Au(788). The behavior of the C 1s peak follows the trend of the analogous peak during the formation of 7-AGNRs on Au(111).[33] As can be observed in Fig. 2a, at the dehalogenation temperature, the C 1s peak shifts from the RT position to lower binding energies due to the formation of the polyanthryl precursor,[6] and it moves to higher binding energies when the cyclodehydrogenation occurs.

The length and relatively good alignment of the 7-AGNRs grown on the kinked Au surface allows one to investigate their electronic structure by ARPES. In fact, the 7-AGNRs' length is sufficiently large to develop a band structure (in contrast to the Au(110) case[38]) and the 7-AGNRs preferential alignment along equivalent [1$\bar{1}$0] directions is comparable to the order obtained on the Au(788) surface. Previous ARPES experiments were done on 7-AGNRs grown on the vicinal Au(788) plane, which exhibited a high ribbon density within its narrow ≈3.8 nm terraces with excellent alignment along the [1$\bar{1}$0] direction, leading to large domains of equally oriented 7-AGNRs.[39] Angle-resolved photoemission bands acquired along the ribbon axis (k_y axis in the present paper) identified downward dispersing bands,[40] and among them, the apparent frontier valence band of the 7-AGNR, with band maximum

at E_{VB1}=-0.7 eV and k_y = 1.47 Å^{-1} (k_y =2π/a with a=4.26 Å), that is, at the center of the GNR's second Brillouin zone. Notably, the electron effective mass extracted from this band dispersion, m^*= 0.21 m_e (where m_e is the electron mass), largely departed from the value found in Fourier-transformed scanning tunneling spectroscopy (FT-STS) measurements, m^*= 0.41 m_e.[41] In a recent work, Senkovskiy and coworkers solved this discrepancy,[34] assigning the band at -0.7 eV to the VB_2 state of the fused 7-AGNRs. As it occurs in other nanostructured systems with laterally-confined 1D electronic states,[42] the spectral density probed in ARPES has a characteristic modulation for each quantum state in the confinement direction, which in the present case of GNRs is the perpendicular direction to the nanoribbon axis (k_x axis). In practice, Senkovskiy et al. showed that for a proper band labeling of GNR bands it is convenient to compare a full ARPES mapping of the 2D (k_y, k_x) momentum space with photoemission calculations.[34] By doing so, they proved that close to the (k_y = 1.5 Å^{-1}, k_x= 0) point, where most of the previous data were acquired, VB_2 dominates and shades VB_1, although strictly at k_x= 0 the emission from VB_2 is mostly suppressed. In contrast, the true frontier VB_1 band (the first valence band) exhibits its maximum spectral density, and it is best resolved with respect to the other 7-AGNR bands, around the (k_y=0, k_x=1.5 Å^{-1}) point of the 2D spectral distribution. After correctly identifying VB_1, they determined its maximum E_{VB1}=-0.87 eV and effective mass m^*= 0.4 m_e, in agreement with FT-STS experiments.

ARPES measurements were carried out in the 7-AGNR-covered Au(16 14 15) surface. The results displayed in Fig. 3 correspond to experiments performed with fixed k_y= 0 in Fig. 3a and k_x= 0 in Fig. 3b. Besides the band at the $\bar{\Gamma}$ point in the second Brillouin zone of the 7-AGNR (k_y=1.5 Å^{-1}) with a maximum at E_{VB1}=-1 eV (see Fig. S5), we unexpectedly detect another band feature dispersing downward around k_y=0, under some remnant surface state intensity. For the latter, the position of the band edge and its effective mass is obtained by line-fitting individual electron distribution curves. The parabolic line follows the resulting E(k_y) data, shown in Fig. 3c, renders E_{VB1} = -0.89 eV and $m^*\approx$0.4 m_e, that is, values close

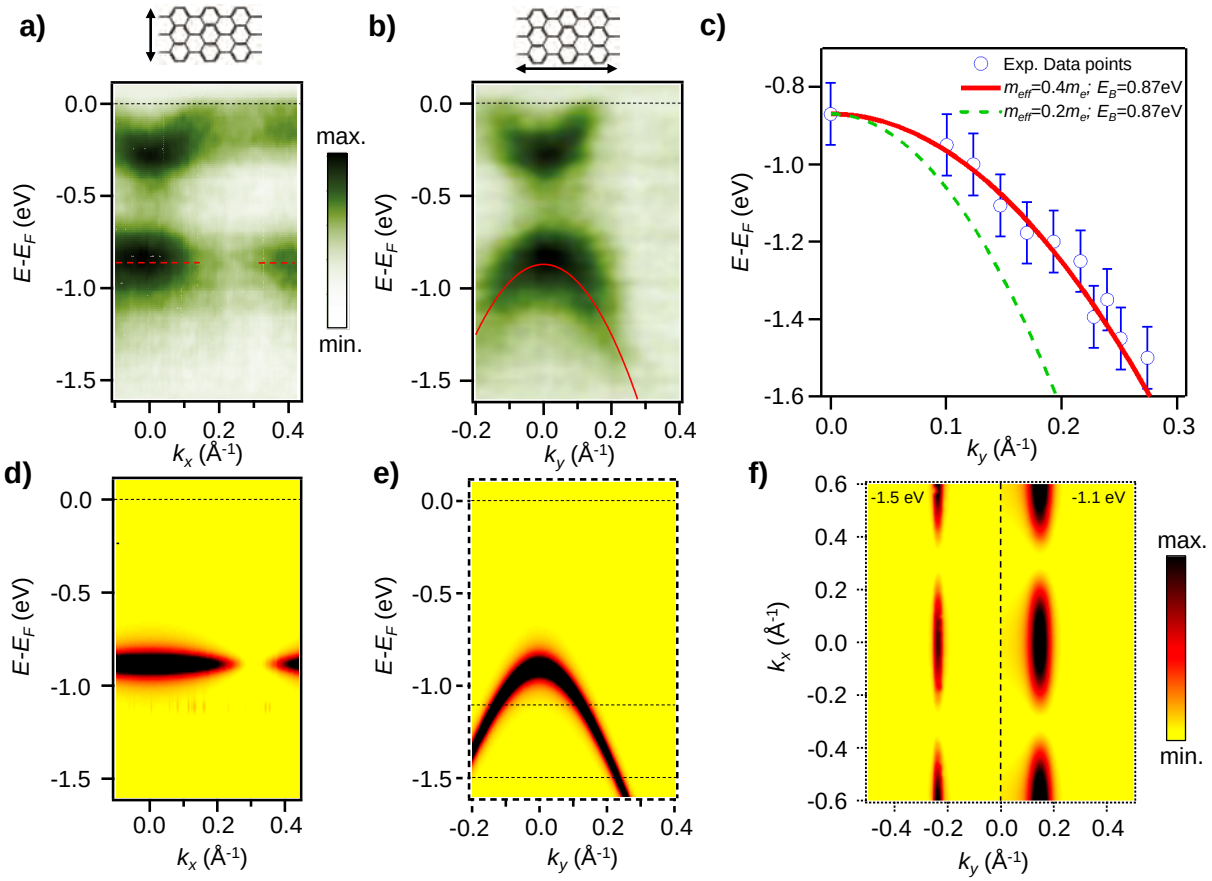

Figure 3: ARPES electronic band structure and EPWE simulations of 7-AGNRs. Band structure of the 7-AGNRs grown on Au(16 14 15) perpendicular (a, k_y=0) and parallel (b, k_x=0) to the average axis direction of the nanoribbons. The Fermi background has been subtracted from the raw data to improve visualization. In (b) one can observe the signature of VB_1 dispersing down from k_x=0, below the Shockley state. (c) Simulated dispersion of the VB_1 electronic band for two different effective mass values: m^*= 0.2 m_e and m^*= 0.4 m_e. The superimposed experimental data resulting from the line-fitting of individual photoemission intensity spectra lie on the band with m^*= 0.4 m_e. The spectral intensities in (a) and (b) coincide with the simulated VB_1 electronic bands of the 7-AGNRs in (d) and (e) respectively. (f) Simulated constant energy cut (k_x vs k_y at E = -1.5 eV and E = -1.1 eV), which highlights the modulation of the photoemission intensity of the VB_1 in the Fourier space.

to those expected for the VB_1 band.[34] Therefore, energies and effective masses for the band features of Fig. 3 point to the presence of the VB_1 band in the 7-AGNRs' first Brillouin zone. Such assignment is in fact corroborated in Figs. 3d-f, where we display the theoretical simulation of the photoemission intensity from free standing 7-AGNRs, as determined from our electron plane wave expansion (EPWE) method.[36] The simulation proves that, at k_x=

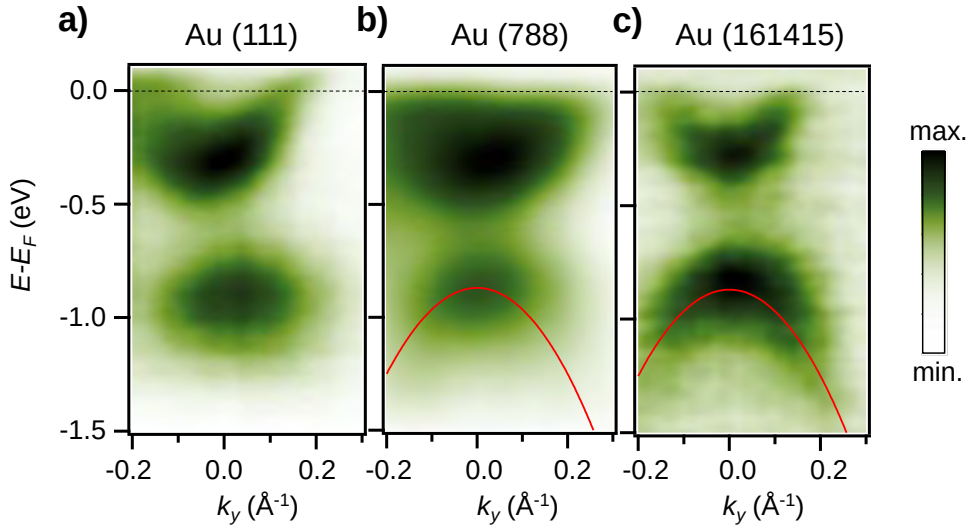

Figure 4: ARPES spectral maps measured on a single layer of 7-AGNRs grown on Au(111) (a), vicinal Au(788) (b) and kinked Au(16 14 15) (c), along the dominant GNR axis k_y. In all cases a downward dispersing GNR-related band is detected around $k_x = 0$, below the Shockley state. We attribute this band to the first occupied GNR band (VB_1), which agrees with our EPWE simulations. In (a) a broad VB_1 dispersion occurs because the GNRs are randomly oriented on the surface. The growth on stepped (b) and kinked (c) surfaces allows a preferential unidirectional ribbon alignment on a macroscopic scale, thus a well-defined VB_1 can be observed.

0 the photoemission spectra is solely determined by the first and second Brillouin zone VB_1 umklapps (see also Fig. S5).

In order to discard that the VB_1 band at $k_x = k_y = 0$ arises due to the particular geometry of the kinked Au(16 14 15) substrate (these effects are discussed in detail in the Supporting Information, Fig. S6), we test its presence in other Au surfaces. Figure 4 shows the ARPES k_y-dispersion maps measured at $k_x = 0$ and in the same experimental conditions on Au(111), Au(788) and Au(16 14 15), all covered with one layer of 7-AGNRs. In all cases a downwards dispersing feature is detected around $k_y = 0$, right below the Shockley state, which we assign to VB_1, according to our simulations. In Au(111) (Fig. 4a) the VB_1 feature appears fuzzy and broad, as expected from randomly oriented GNRs. The improved unidirectional alignment of the nanoribbons for Au(788) and Au(16 15 14) results in better-defined VB_1 dispersions of Figs. 4b and 4c, respectively.

Our experimental observations are in agreement with both EPWE and DFT calculations[34]

(see Fig. S7). The predicted VB_1 features at normal emission are quite faint in both cases, so their spectral weight is expected to be very limited compared to other positions in momentum space, e.g. (k_x, k_y)=(1.5, 0) $Å^{-1}$. Thus, experimental observation of this band must require controlled sample quality (growth perfection and high surface coverage), use of low photon energy (to enhance the carbon $2p$ orbital cross-section), and proper selection of the set-up geometry (light incidence and polarization).[43]

The question arises why this band has never been observed in previous ARPES experiments performed on Au(788) using similar experimental acquisition geometries. The most plausible reason behind this difference is in the use of different photon energies, beam incidence or light polarization conditions for the ARPES acquisition. Such difference suggests that a significant energy dependent cross section must be present for these GNRs. Data shown in Figs. 3 and 4 were acquired with a photon energy of 21.2 eV and 88% p-polarized light using a laboratory source, while previous measurements were undertaken with energies between 32 eV and 50 eV with mainly horizontal polarization conditions at synchrotron radiation facilities.[34,40,44,45] We infer that it is a sum of factors where the photon energy and light polarization vectors favors the observation of the inherently weak band at $\bar{\Gamma}$. Such photoemission matrix element effects most likely dim its intensity at higher photon energies, which could be the reason why it has not been reported so far.

Conclusions

In summary, we have synthesized 7-AGNRs on the Au(16 14 15) kinked surface. Due to the high temperature ribbons growth, which likely favours Au adatoms diffusion away from the kinked steps, the surface undergoes a nanoscale step-edge reshaping, and an atomic-scale missing row reconstruction within terraces. The catalytic activity of the surface lowers the dehalogenation temperature with respect to the flat Au(111). The preferential alignment of the 7-AGNRs on the reconstructed Au(16 14 15) along the two equivalent close packed

directions allows for well-resolved standard ARPES measurements using laboratory sources. The low photon energy and the measuring geometry employed, results in the observation of the occupied frontier band of the 7-AGNRs at the $\bar{\Gamma}$ point in their first Brillouin zone, which in turn permits the unambiguous determination of the band maximum and the carrier effective mass, that agree with results published elsewhere.

Supporting Information

The Supporting Information includes: a sketch of the ARPES setup used in our experiments; an analysis of the orientation and length distribution of 7-AGNRs on the Au(16 14 15) surface; STM image line profile of the (2×1) Au terrace reconstruction; the comparison of LEED patterns of clean and 7-AGNRs covered Au(16 14 15); the explanation of the extended band structure of the 7-AGNRs grown on Au(16 14 15) in the direction parallel to the axis of the nanoribbons; the discussion of the origin of the appearance of the band in $\bar{\Gamma}$ and comparison of DFT and EPWE simulations of (k_x vs k_y) maps at -1.1 eV.

Acknowledgement

The authors acknowledge financial support from the Spanish Ministry of Science and Innovation (MAT2016-78293-C6), from the Basque Government (IT-1255-19), from the European Regional Development Fund (ERDF) under the program Interreg V-A España-Francia-Andorra (Contract No. EFA 194/16 TNSI) and from the European Research Council (grant agreement No. 635919).

References

(1) Bennet, P.; Pedramrazi, Z.; Madani, A.; Chen, Y.-C.; de Oteyza, D.; Chen, C.; Fischer, F.; Crommie, M.; Bokor, J. Bottom-Up Graphene Nanoribbon Field-Effect Transistors. *App. Phys. Lett.* **2013**, *103*, 253114.

(2) Linas, J.; Fairbrother, A.; Borin Barin, G.; Shi, W.; Lee, K.; Wu, S.; Yong Choi, B.; Braganza, R.; Lear, J.; Kau, N. et al. Short-Channel Field Effect Transistor with 9-Atom and 13-Atom Wide Graphene Nanoribbons. *Nat. Comm.* **2017**, *8*, 633.

(3) Passi, V.; Gahoi, A.; Senkovskiy, B. V.; Haberer, D.; Fischer, F. R.; Grüneis, A.; Lemme, M. C. Field-Effect Transistors Based on Networks of Highly Aligned, Chemically Synthesized N = 7 Armchair Graphene Nanoribbons. *ACS Applied Materials & Interfaces* **2018**, *10*, 9900–9903.

(4) Kargar, A.; Lee, C. Graphene Nanoribbon Schottky Diodes Using Asymmetric Contacts. **2009**, 243–245.

(5) Naeemi, A.; Meindl, J. D. Conductance Modeling for Graphene Nanoribbon (GNR) Interconnects. *IEEE Electron Device Letters* **2007**, *28*, 428–431.

(6) Cai, J.; Ruffieux, R., Pascaland Jaafar; Bieri, M.; Braun, T.; Blankenburg, S.; Muoth, M.; Seitsonen, A. P.; Saleh, M.; Feng, X.; Müllen, K. et al. Atomically Precise Bottom-up Fabrication of Graphene Nanoribbons. *Nature* **2010**, *466*, 470–473.

(7) Talirz, L.; Ruffieux, P.; Fasel, R. On-Surface Synthesis of Atomically Precise Graphene Nanoribbons. *Advanced Materials* **2016**, *28*, 6222–6231.

(8) Ruffieux, P.; Wang, S.; Yang, B.; Sánchez-Sánchez, C.; Liu, J.; Dienel, T.; Talirz, L.; Shinde, P.; Pignedoli, C. A.; Passerone, D. et al. On-Surface Synthesis of Graphene Nanoribbons with Zigzag Edge Topology. *Nature* **2016**, *531*, 489 – 492.

(9) de Oteyza, D. G.; Garcìa-Lekue, A.; Vilas-Varela, M.; Merino-Dìez, N.; Carbonell-Sanromà, E.; Corso, M.; Vasseur, G.; Rogero, C.; Guitiàn, E.; Pascual, J. I. et al. Substrate-Independent Growth of Atomically Precise Chiral Graphene Nanoribbons. *ACS Nano* **2016**, *10*, 9000–9008.

(10) Merino-Dìez, N.; Garcia-Lekue, A.; Carbonell-Sanromà, E.; Li, J.; Corso, M.; Colazzo, L.; Sedona, F.; Sànchez-Portal, D.; Pascual, J. I.; de Oteyza, D. G. Width-Dependent Band Gap in Armchair Graphene Nanoribbons Reveals Fermi Level Pinning on Au(111). *ACS Nano* **2017**, *11*, 11661–11668.

(11) Chen, Y.-C.; de Oteyza, D. G.; Pedramrazi, Z.; Chen, C.; Fischer, F. R.; Crommie, M. F. Tuning the Band Gap of Graphene Nanoribbons Synthesized from Molecular Precursors. *ACS Nano* **2013**, *7*, 6123–6128.

(12) Abdurakhmanova, N.; Amsharov, N.; Stepanow, S.; Jansen, M.; Kern, K.; Amsharov, K. Synthesis of Wide Atomically Precise Graphene Nanoribbons from Para-Oligophenylene Based Molecular Precursor. *Carbon* **2014**, *77*, 1187 – 1190.

(13) Kimouche, A.; Ervasti, M. M.; Drost, R.; Halonen, S.; Harju, A.; Joensuu, P. M.; Sainio, J.; Liljeroth, P. Ultra-Narrow Metallic Armchair Graphene Nanoribbons. *Nature Communications* **2015**, *6*, 10177.

(14) Zhang, H.; Lin, H.; Sun, K.; Chen, L.; Zagranyarski, Y.; Aghdassi, N.; Duhm, S.; Li, Q.; Zhong, D.; Li, Y. et al. On-Surface Synthesis of Rylene-Type Graphene Nanoribbons. *Journal of the American Chemical Society* **2015**, *137*, 4022–4025.

(15) Talirz, L.; Söde, H.; Dumslaff, T.; Wang, S.; Sanchez-Valencia, J. R.; Liu, J.; Shinde, P.; Pignedoli, C. A.; Liang, L.; Meunier, V. et al. On-Surface Synthesis and Characterization of 9-Atom Wide Armchair Graphene Nanoribbons. *ACS Nano* **2017**, *11*, 1380–1388.

(16) Kawai, S.; Saito, S.; Osumi, S.; Yamaguchi, S.; Foster, A. S.; Spijker, P.; Meyer, E. Atomically Controlled Substitutional Boron-Doping of Graphene Nanoribbons. *Nature Communications* **2015**, *6*, 8098.

(17) Cloke, R. R.; Marangoni, T.; Nguyen, G. D.; Joshi, T.; Rizzo, D. J.; Bronner, C.; Cao, T.; Louie, S. G.; Crommie, M. F.; Fischer, F. R. Site-Specific Substitutional Boron Doping of Semiconducting Armchair Graphene Nanoribbons. *Journal of the American Chemical Society* **2015**, *137*, 8872–8875.

(18) Kawai, S.; Nakatsuka, S.; Hatakeyama, T.; Pawlak, R.; Meier, T.; Tracey, J.; Meyer, E.; Foster, A. S. Multiple Heteroatom Substitution to Graphene Nanoribbon. *Science Advances* **2018**, *4*, eaar7181.

(19) Nguyen, G. D.; Toma, F. M.; Cao, T.; Pedramrazi, Z.; Chen, C.; Rizzo, D. J.; Joshi, T.; Bronner, C.; Chen, Y.-C.; Favaro, M. et al. Bottom-Up Synthesis of N = 13 Sulfur-Doped Graphene Nanoribbons. *The Journal of Physical Chemistry C* **2016**, *120*, 2684–2687.

(20) Wang, X.-Y.; Urgel, J. I.; Barin, G. B.; Eimre, K.; Di Giovannantonio, M.; Milani, A.; Tommasini, M.; Pignedoli, C. A.; Ruffieux, P.; Feng, X. et al. Bottom-Up Synthesis of Heteroatom-Doped Chiral Graphene Nanoribbons. *Journal of the American Chemical Society* **2018**, *140*, 9104–9107.

(21) Cai, J.; Pignedoli, C. A.; Talirz, L.; Ruffieux, P.; Söde, H.; Liang, L.; Meunier, V.; Berger, R.; Li, R.; Feng, X. et al. Graphene Nanoribbons Heterojunctions. *Nature Nanotechnology* **2014**, *9*, 896–900.

(22) Bronner, C.; Stremlau, S.; Gille, M.; Brauße, F.; Haase, A.; Hecht, S.; Tegeder, P. Aligning the Band Gap of Graphene Nanoribbons by Monomer Doping. *Angewandte Chemie International Edition* **2013**, *52*, 4422–4425.

(23) Durr, R. A.; Haberer, D.; Lee, Y.-L.; Blackwell, R.; Kalayjian, A. M.; Marangoni, T.; Ihm, J.; Louie, S. G.; Fischer, F. R. Orbitally Matched Edge-Doping in Graphene Nanoribbons. *Journal of the American Chemical Society* **2018**, *140*, 807–813.

(24) Carbonell-Sanromà, E.; Hieulle, J.; Vilas-Varela, M.; Brandimarte, P.; Iraola, M.; Barragán, A.; Li, J.; Abadia, M.; Corso, M.; Sánchez-Portal, D. et al. Doping of Graphene Nanoribbons via Functional Group Edge Modification. *ACS Nano* **2017**, *11*, 7355–7361.

(25) Nguyen, G. D.; Tsai, H. Z.; Omrani, A. A.; Marangoni, T.; Wu, M.; Rizzo, D. J.; Rodgers, G. F.; Cloke, R. R.; Durr, R. A.; Sakai, Y. et al. Atomically Precise Graphene Nanoribbon Heterojunctions from a Single Molecular Precursor. *Nature Nanotechnology* **2017**, *12*, 1077–1082.

(26) Moreno, C.; Paradinas, M.; Vilas-Varela, M.; Panighel, M.; Ceballos, G.; Peña, D.; Mugarza, A. On-Surface Synthesis of Superlattice Arrays of Ultra-Long Graphene Nanoribbons. *Chem. Commun.* **2018**, *54*, 9402–9405.

(27) Senkovskiy, B. V.; Pfeiffer, M.; Alavi, S. K.; Bliesener, A.; Zhu, J.; Michel, S.; Fedorov, A. V.; German, R.; Hertel, D.; Haberer, D. et al. Making Graphene Nanoribbons Photoluminescent. *Nano Letters* **2017**, *17*, 4029–4037.

(28) Ohtomo, M.; Sekine, Y.; Hibino, H.; Yamamoto, H. Graphene Nanoribbon Field-Effect Transistors Fabricated by Etchant-Free Transfer from Au(788). *Applied Physics Letters* **2018**, *112*, 021602.

(29) Saywell, A.; Schwarz, J.; Hecht, S.; Grill, L. Polymerization on Stepped Surfaces: Alignment of Polymers and Identification of Catalytic Sites. *Angewandte Chemie* **2012**, *124*, 5186–5190.

(30) Ortega, J. E.; Vasseur, G.; Piquero-Zulaica, I.; Matencio, S.; Valbuena, M. A.; Rault, J. E.; Schiller, F.; Corso, M.; Mugarza, A.; Lobo-Checa, J. Structure and Elec-

tronic States of Vicinal Ag(111) Surfaces with Densely Kinked Steps. *New Journal of Physics* **2018**, *20*, 073010.

(31) Piquero-Zulaica, I.; Garcia-Lekue, A.; Colazzo, L.; Krug, C. K.; Mohammed, M. S. G.; Abd El-Fattah, Z. M.; Gottfried, J. M.; de Oteyza, D. G.; Ortega, J. E.; Lobo-Checa, J. Electronic Structure Tunability by Periodic meta-Ligand Spacing in One-Dimensional Organic Semiconductors. *ACS Nano* **2018**, *12*, 10537–10544.

(32) Greber, T.; Šljivančanin Ž.,; Schillinger, R.; Wider, J.; Hammer, B. Chiral Recognition of Organic Molecules by Atomic Kinks on Surfaces. *Phys. Rev. Lett.* **2006**, *96*, 056103.

(33) Massimi, L.; Ourdjini, O.; Lafferentz, L.; Koch, M.; Grill, L.; Cavaliere, E.; Gavioli, L.; Cardoso, C.; Prezzi, D.; Molinari, E. et al. Surface-Assisted Reactions toward Formation of Graphene Nanoribbons on Au(110) Surface. *The Journal of Physical Chemistry C* **2015**, *119*, 2427–2437.

(34) Senkovskiy, B. V.; Usachov, D. Y.; Fedorov, A. V.; Haberer, D.; Ehlen, N.; Fischer, F. R.; Grüneis, A. Finding the Hidden Valence Band of N = 7 Armchair Graphene Nanoribbons with Angle-Resolved Photoemission Spectroscopy. *2D Materials* **2018**, *5*, 035007.

(35) Horcas, I.; Fernández, R.; Gómez-Rodríguez, J. M.; Colchero, J.; Gómez-Herrero, J.; Baro, A. M. WSXM: A Software for Scanning Probe Microscopy and a Tool for Nanotechnology. *Review of Scientific Instruments* **2007**, *78*, 013705.

(36) Abd El-Fattah, Z. M.; Kher-Elden, M. A.; Piquero-Zulaica, I.; de Abajo, F. J. G.; Ortega, J. E. Graphene: Free Electron Scattering within an Inverted Honeycomb Lattice. *Phys. Rev. B* **2019**, *99*, 115443.

(37) Basagni, A.; Sedona, F.; Pignedoli, C. A.; Cattelan, M.; Nicolas, L.; Casarin, M.; Sambi, M. Molecules–Oligomers–Nanowires–Graphene Nanoribbons: A Bottom-Up

Stepwise On-Surface Covalent Synthesis Preserving Long-Range Order. *Journal of the American Chemical Society* **2015**, *137*, 1802–1808.

(38) Della Pia, A.; Avvisati, G.; Ourdjini, O.; Cardoso, C.; Varsano, D.; Prezzi, D.; Ferretti, A.; Mariani, C.; Betti, M. G. Electronic Structure Evolution during the Growth of Graphene Nanoribbons on Au(110). *The Journal of Physical Chemistry C* **2016**, *120*, 7323–7331.

(39) Linden, S.; Zhong, D.; Timmer, A.; Aghdassi, N.; Franke, J. H.; Zhang, H.; Feng, X.; Müllen, K.; Fuchs, H.; Chi, L. et al. Electronic Structure of Spatially Aligned Graphene Nanoribbons on Au(788). *Phys. Rev. Lett.* **2012**, *108*, 216801.

(40) Ruffieux, P.; Cai, J.; Plumb, N. C.; Patthey, L.; Prezzi, D.; Ferretti, A.; Molinari, E.; Feng, X.; Müllen, K.; Pignedoli, C. A. et al. Electronic Structure of Atomically Precise Graphene Nanoribbons. *ACS Nano* **2012**, *6*, 6930–6935.

(41) Söde, H.; Talirz, L.; Gröning, O.; Pignedoli, C. A.; Berger, R.; Feng, X.; Müllen, K.; Fasel, R.; Ruffieux, P. Electronic Band Dispersion of Graphene Nanoribbons via Fourier-Transformed Scanning Tunneling Spectroscopy. *Phys. Rev. B* **2015**, *91*, 045429.

(42) Mugarza, A.; Ortega, J. E.; Himpsel, F. J.; García de Abajo, F. J. Measurement of Electron Wave Functions and Confining Potentials via Photoemission. *Phys. Rev. B* **2003**, *67*, 081404.

(43) Gierz, I.; Henk, J.; Höchst, H.; Ast, C. R.; Kern, K. Illuminating the dark corridor in graphene: Polarization dependence of angle-resolved photoemission spectroscopy on graphene. *Phys. Rev. B* **2011**, *83*, 121408.

(44) Senkovskiy, B. V.; Fedorov, A. V.; Haberer, D.; Farjam, M.; Simonov, K. A.; Preobrajenski, A. B.; Mårtensson, N.; Atodiresei, N.; Caciuc, V.; Blügel, S. et al. Semiconductor-to-Metal Transition and Quasiparticle Renormalization in Doped Graphene Nanoribbons. *Advanced Electronic Materials* **2017**, *3*, 1600490.

(45) Simonov, K. A.; Vinogradov, N. A.; Vinogradov, A. S.; Generalov, A. V.; Svirskiy, G. I.; Cafolla, A. A.; Mårtensson, N.; Preobrajenski, A. B. Effect of Electron Injection in Copper-Contacted Graphene Nanoribbons. *Nano Research* **2016**, *9*, 2735–2746.

Graphical TOC Entry